Journal of Structural Geology, Vol. 8 No. 5, pp. 543 to 562, 1986
Printed in Great Britain

0191-8141/86 $3.00+0.00
Pergamon Journals Ltd

Step-wise growth of biotite porphyroblasts in pelitic schists of the western Lys-Caillaouas massif (Pyrenees)

G. S. LISTER*, J. N. BOLAND, and H. J. ZWART

Department of Structural Geology, Institute for Earth Sciences,
University of Utrecht, 3508 TA Utrecht, The Netherlands

(*Received* 25 *July* 1983; *accepted in revised form* 14 *June* 1985)

Abstract—Detailed optical and electron microscope (SEM and TEM) examination of biotite blasts from pelitic schists of the western Lys-Caillaouas massif in the Pyrenees reveals a variety of microstructures suggesting growth of the blasts before and after a thermal peak during the D_2 deformation. In the early stages of growth the biotites had (001) at high angles to S_1, and they appear to have existed as thin (001) parallel plates. In many cases blastesis is suggested to have involved growth of the biotites into their own continuously dilating pressure shadows. Inclusions with dentate grain boundaries, banded structures, and 'radiator-fin' intergrowths suggest a mechanism analogous to the Ramsay crack–seal model for vein formation, but here involving step-wise dilation of a pressure-shadow cavity into which the adjacent blast itself was growing.

INTRODUCTION

THIS PAPER concerns growth microstructures in biotite blasts from deformed Cambro-Ordovician metapelites belonging to the western part of the Lys-Caillaouas metamorphic aureole (Fig. 1) in the axial zone of the Pyrenees. The rocks were collected from outcrops in the valley of the Rioumajou, France. The study has been performed because the microstructures contain information, the interpretation of which may lead to a more fundamental understanding of the physical processes involved in blastesis.

Regional structure

The Lys granite is a composite intrusive body containing a megacryst granite, a leucocratic muscovite-bearing granite and a quartz diorite. The body has the form of a sheet, and from the geometry of large inclusions of mica schists (up to 100 m thick) the sheet appears to be folded by major EW-trending antiforms and synforms.

Clin (1959) and Trouiller (1976) note that the structure of the Rioumajou valley is affected by a tight kilometer-scale (D_1) anticline. However the structure is more complex than has been previously described. There is a cleavage (S_1) which is the result of the earlier deformation(s) (D_1). This has been affected by subsequent deformation(s) (D_2 and later) as shown in Fig. 2. At the northern and southern ends of the valley, and on the ridge to the east, S_1 or its enveloping surface is usually steeply dipping. The effects of D_2 are seen as abundant small-scale folds and crenulations, with S_2 defined by frequently developed (axial plane) crenulation cleavages. In the valley near Frédancon however, there is a zone where foliations are shallow dipping. Field observations linked with microstructural analysis indicate that here S_1 has been transposed into parallelism with S_2 by intense isoclinal folding and shear. Relicts of crenulated S_1 are preserved in large andalusite and staurolite porphyroblasts, and in the adjacent strain shadows, as shown in Fig. 2.

The D_2 transposition zone defines an open antiform and, as can be seen in Fig. 2, this same antiform is reflected in changes in the attitudes of S_2 axial-plane structures in the surrounding zones of steeply dipping S_1. This antiformal structure developed during or after D_2. It has a WNW fold axis, parallel to D_2 fold axes in the Frédancon zone, with the same trend as the large open folds in the granite body of Lys-Caillaouas.

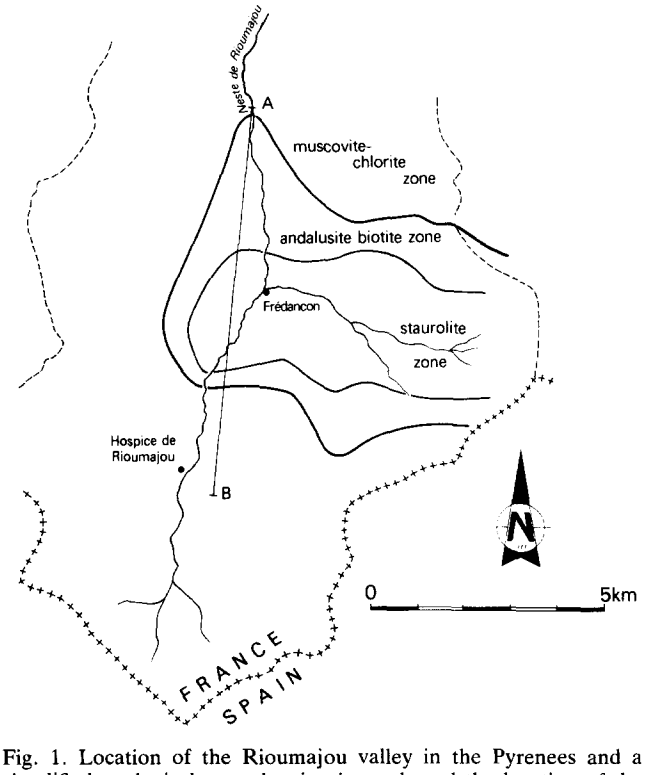

Fig. 1. Location of the Rioumajou valley in the Pyrenees and a simplified geological map showing isograds and the location of the Frédancon transposition zone.

* Present Address: Bureau of Mineral Resources, Geology and Geophysics, P.O. Box 378, Canberra City, 2601, Australia.

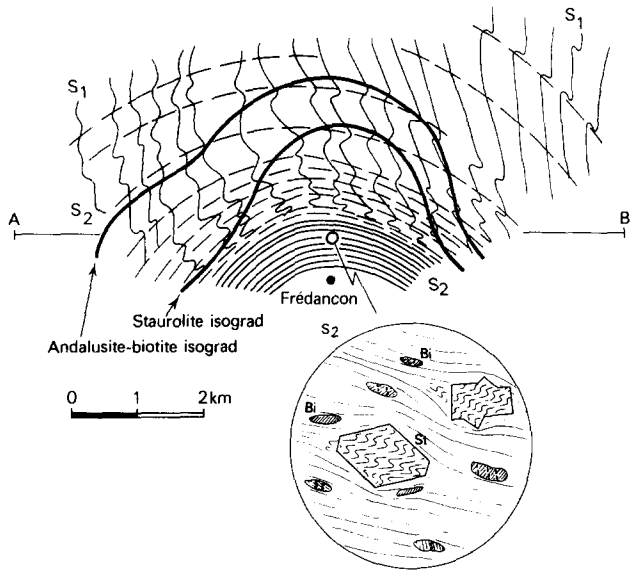

Fig. 2. Schematic cross-section N–S through the Rioumajou valley showing the Frédancon anticline, the development of S_2 and the zone of D_2 transposition. Note the relations between foliations and porphyroblasts.

Metamorphism

The envelope of mica schists around the Lys granite contains abundant alumino-silicates, including chloritoid, staurolite, andalusite, cordierite and sillimanite. The low-pressure high-temperature metamorphism thus implied has the characteristics of a regional metamorphism *sensu stricto* (Zwart 1962, 1963, 1979). For example, blastesis of the various alumino-silicates in part predates intrusion of the Lys granite to its present structural level, and over a considerable part of the area the rapid increase of metamorphic temperatures downwards is not directly associated with the presence of igneous rocks. It is likely that we are dealing with an area in which deformation, metamorphism, migmatization and anatexis took place under conditions associated with abnormally high geothermal gradients.

In the valley of the Rioumajou, metamorphic grade rises sharply downwards. Isograds appear to be affected by the major open antiform. According to Zwart (1963) conditions at the peak of metamorphism were approximately 1.5–2 kb (150–200 Mpa), 550–600°C. Using a density of 2.8×10^3 kg m^{-3}, this implies depths of around 5.5–7.2 km, and a (palaeo) geothermal gradient locally as high as 80–110°C km^{-1}.

This study is confined to biotite blasts which grew under greenschist and lower amphibolite facies conditions, just above the upper part of the Frédancon zone, in areas *not* affected by high D_2 strain (see Fig. 2).

Deformation

Many of the deformation features in these rocks can be explained in terms of local mass removal via a 'pressure solution' process, mass transfer through a grain boundary network involving fluid or a fluid film, and then local mass addition in dilation sites, via the process of mineral growth. The term 'pressure solution' is used to imply preferential dissolution at interfaces subjected to relatively high normal stress during deformation (cf. Rutter 1983). Local mass removal took place at such interfaces (e.g. Figs. 3a & d) as evidenced by increased concentrations of 'insoluble residues' on boundaries which are approximately parallel to the foliation trace. Mass addition took place in dilation sites, for example in the hinges of crenulations, or in pressure-shadows and cleavage-split pull-apart structures.

Timing relationships

Blasts of andalusite, biotite and staurolite in general overgrew a previously existing cleavage (S_1). In many cases the blasts overgrew crenulations. The process of crenulation continued after blastesis ceased, and in the Frédancon zone considerable D_2 strains then accumulated. This suggests that blastesis occurred during the early stages of D_2. However, in most places outside the Frédancon zone, the amount of strain imposed during D_2 subsequent to blastesis probably does not exceed 30% additional shortening.

If blastesis marks the peak of metamorphism, then D_2 is a deformation that occurred partially under prograde conditions and partially under retrograde conditions.

BLASTESIS AND THE ATTITUDE OF S_1 TO THE D_2 FLOW FIELD

The principal variation of microstructures in the biotite blasts depends on whether the pre-existing foliation (S_1) was in the extension field or the shortening field of the second deformation (D_2), during growth of the blasts. If S_1 was in the D_2 shortening field it became folded and crenulated, the crenulations becoming tighter with increasing strain. Biotite blasts which grew during early D_2 preserved the enclosed crenulations at a juvenile stage of development (Fig. 3a). Deformation continued in the matrix causing S_2 to warp around some of the blasts. Stylolites (mass removal surfaces) occasionally formed on the sides of blasts perpendicular to S_1, while crenulations began to differentiate, leading to concentrations of opaques, including graphite (Fig. 3a, see arrow).

If S_1 was in the D_2 extension field, pressure-shadows developed on the sides of blasts perpendicular to S_1 and local mass removal often led to concentrations of opaques near the sides of blasts parallel to S_1 (Figs. 3c & d). Occasionally the blasts were pulled apart on cleavage-splits (Fig. 3c), or as the result of boudinage. Most of the blasts that grew under these conditions contain *S*- or *Z*-shaped inclusion trails (e.g. Figs. 3b & d, 4a & b).

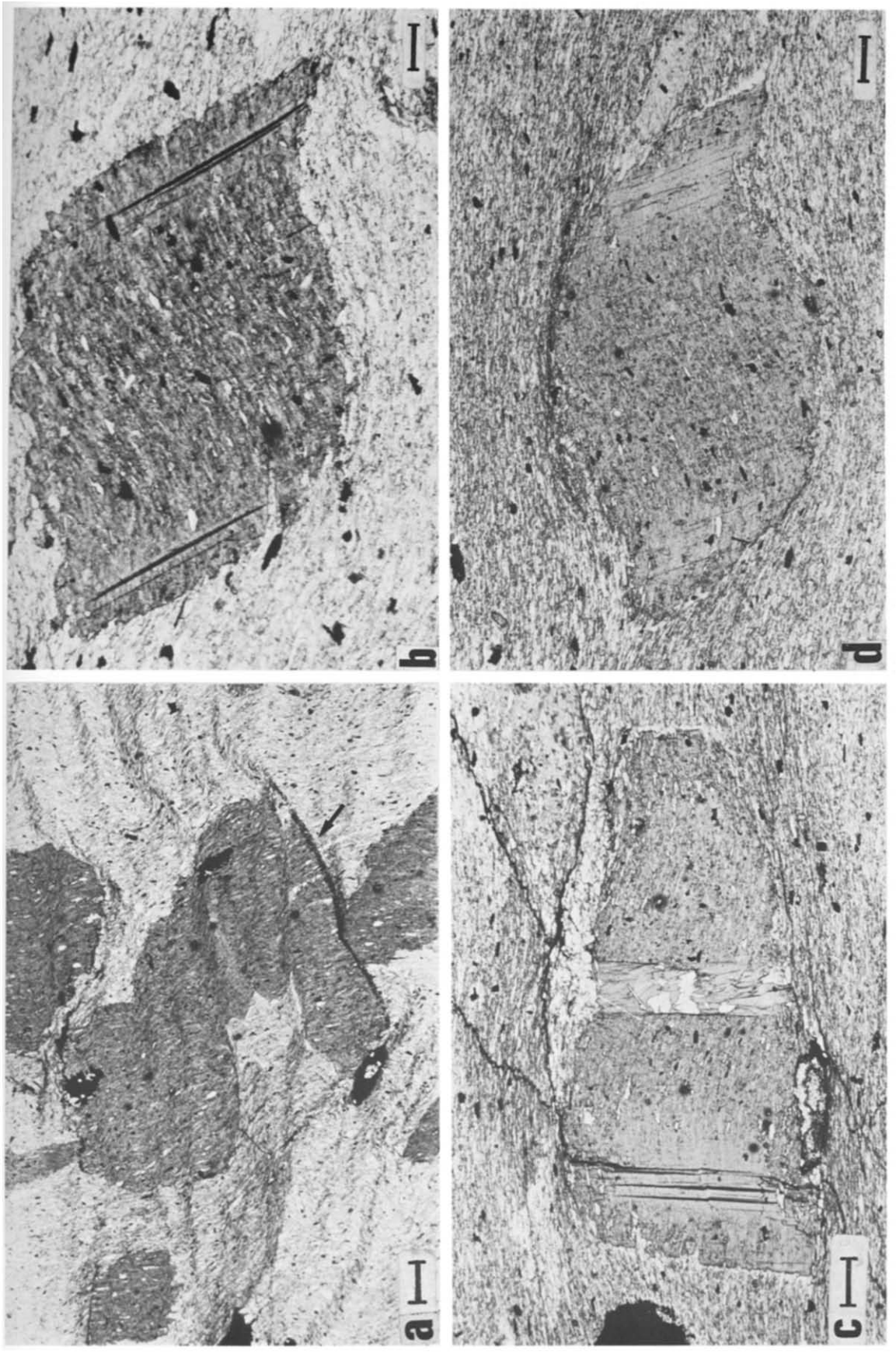

Fig. 3. (a) If S_1 remained in the D_2 shortening field, biotites overgrew crenulations. Crenulation continued after blastesis ceased. (b–d) If S_1 remained in the D_2 extension field, biotites with curved inclusion trails developed. Cleavage-split pull-aparts (c) also developed as well as pressure-shadows and stylolitic residues (d). Note the pyrite lamellae (b, c) and the pyrite microveinlet (c). The arrow in (a) indicates the position of stylolitic residue. Scale bars are: (a) 260 μm; (b) 110 μm; (c, d) 200 μm.

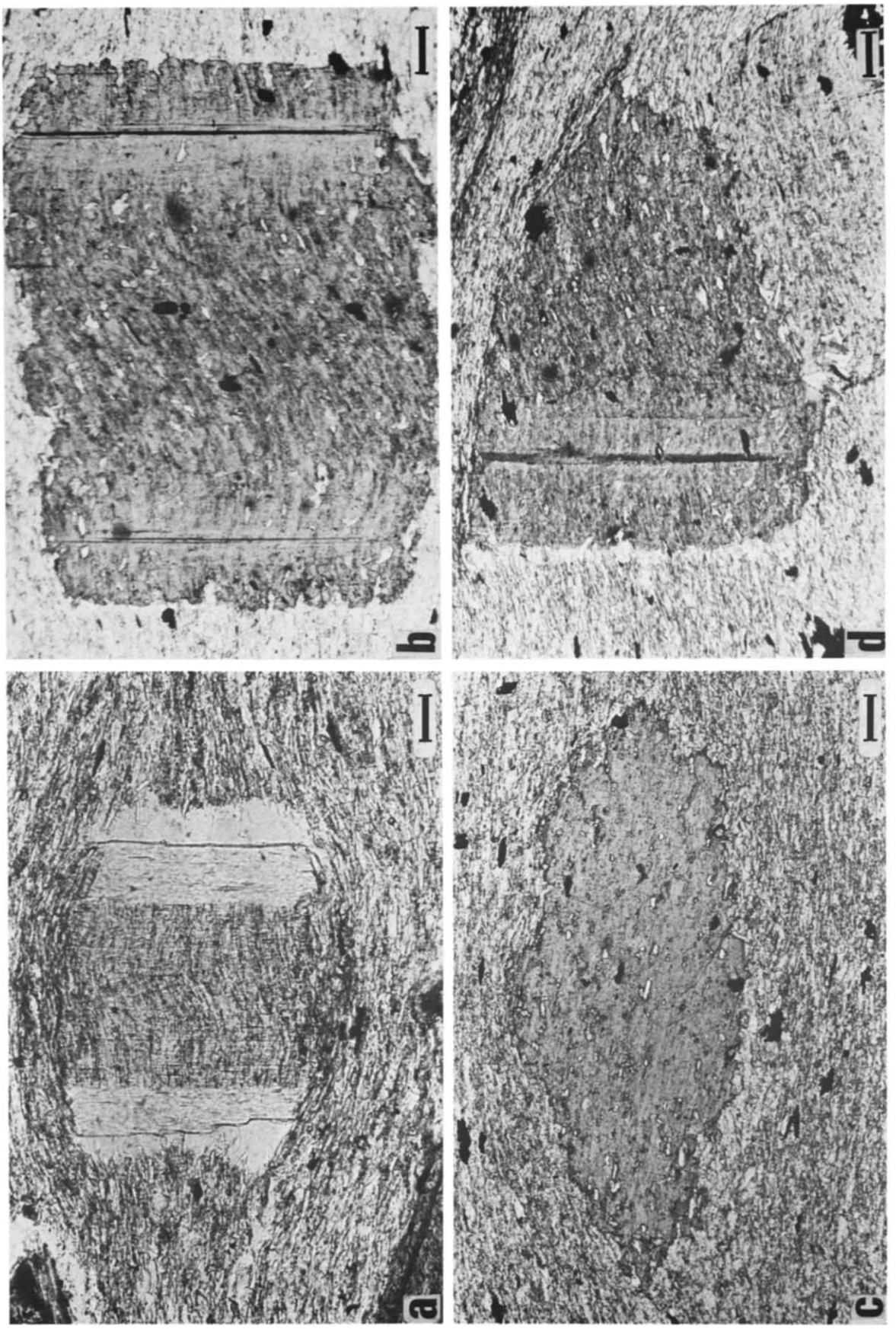

Fig. 4. Biotite blasts with tabular habits are illustrated. The biotite (001) in such blasts was intially inclined 40–60° to S_1, leaning back against the operative shear sense. The blasts have been rotated to their present attitude, with S_1 almost perpendicular to the biotite (001). (a, b) Note paired 'clear' zones and pressure shadows at the (001) terminations of the blasts. (c, d) Microstructural variation related to two-dimensional cut effects is shown (see also Fig. 5). In (c) the biotite (001) is parallel to the section, and in (d) the (001) plane dips 40–50° into the section (trace vertical). Scale bars: (a) 130 μm; (b–d) 150 μm.

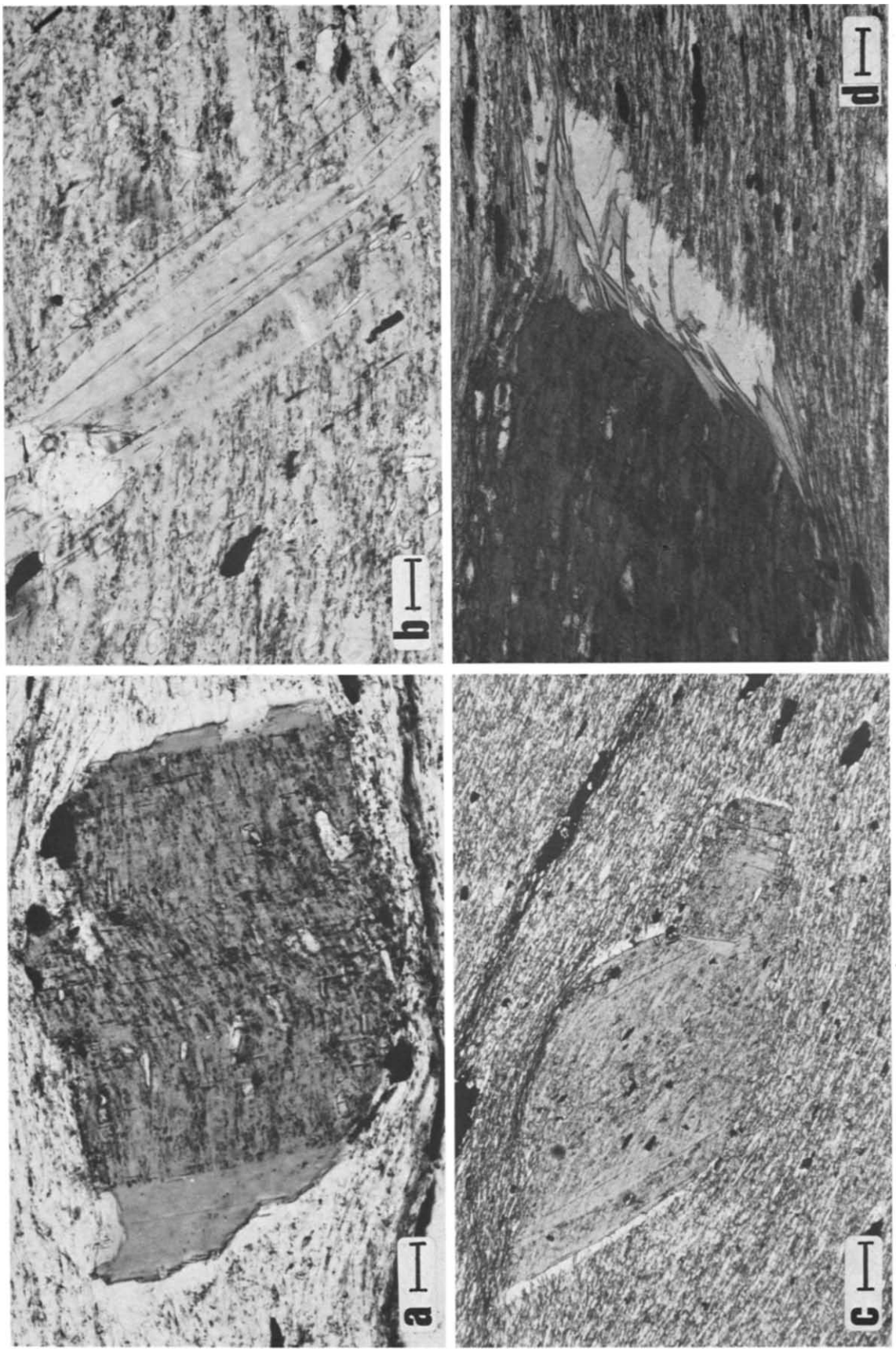

Fig. 6. Pressure-shadows, 'clear' zones, and cleavage-split pull-aparts in the biotite blasts. In (a) the blast has grown into its own pressure-shadow. In (b) a cleavage split pull-apart has sheets of biotite containing inclusions torn off from the wall during dilation, overgrown by optically clear biotite. In (c) two grains have slid apart and clear biotite has formed in the resultant dilation site. In (d) chlorites growing into a quartz-filled pressure shadow are shown with the chlorite (001) initially within 20° of the biotite (001). Scale bars: (a) 50 μm; (b) 40 μm; (c) 20 μm and (d) 40μm.

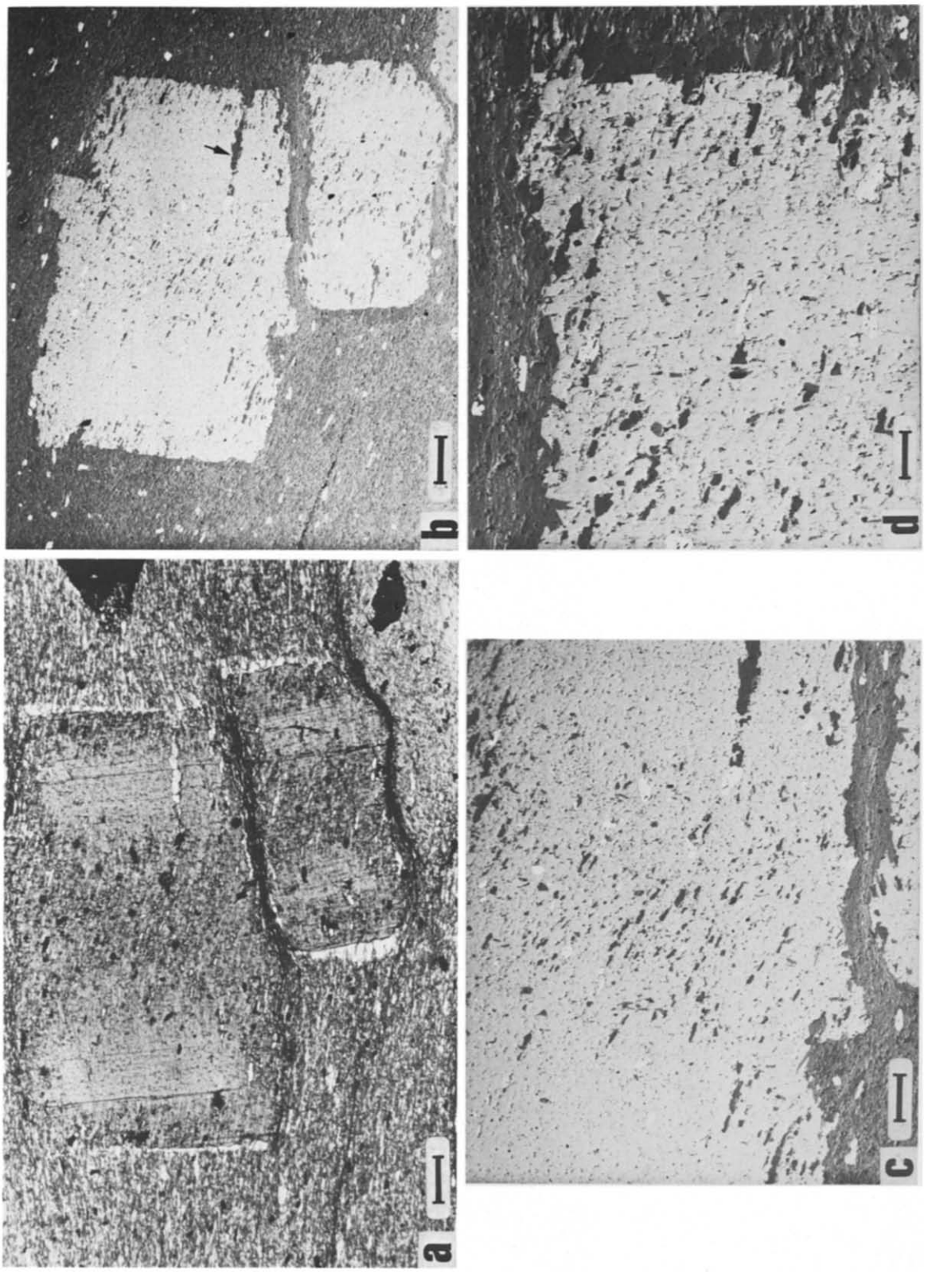

Fig. 7. The optical micrograph (a) is to be contrasted with the Z-number contrast SEM image (b). This is a tabular blast with pressure-shadows and stylolitic residues. Sense-of-shear is dextral. In (b) the arrow indicates a dentate quartz inclusion, also visible in (c). Note form of inclusions in SEM images (c, d) with numerous surfaces parallel to the biotite (001). Diagram (d) is view of upper right of lower blast in (b). Scale bars: (a) 480 μm; (b) 400 μm; (c) 200 μm and (d) 100 μm.

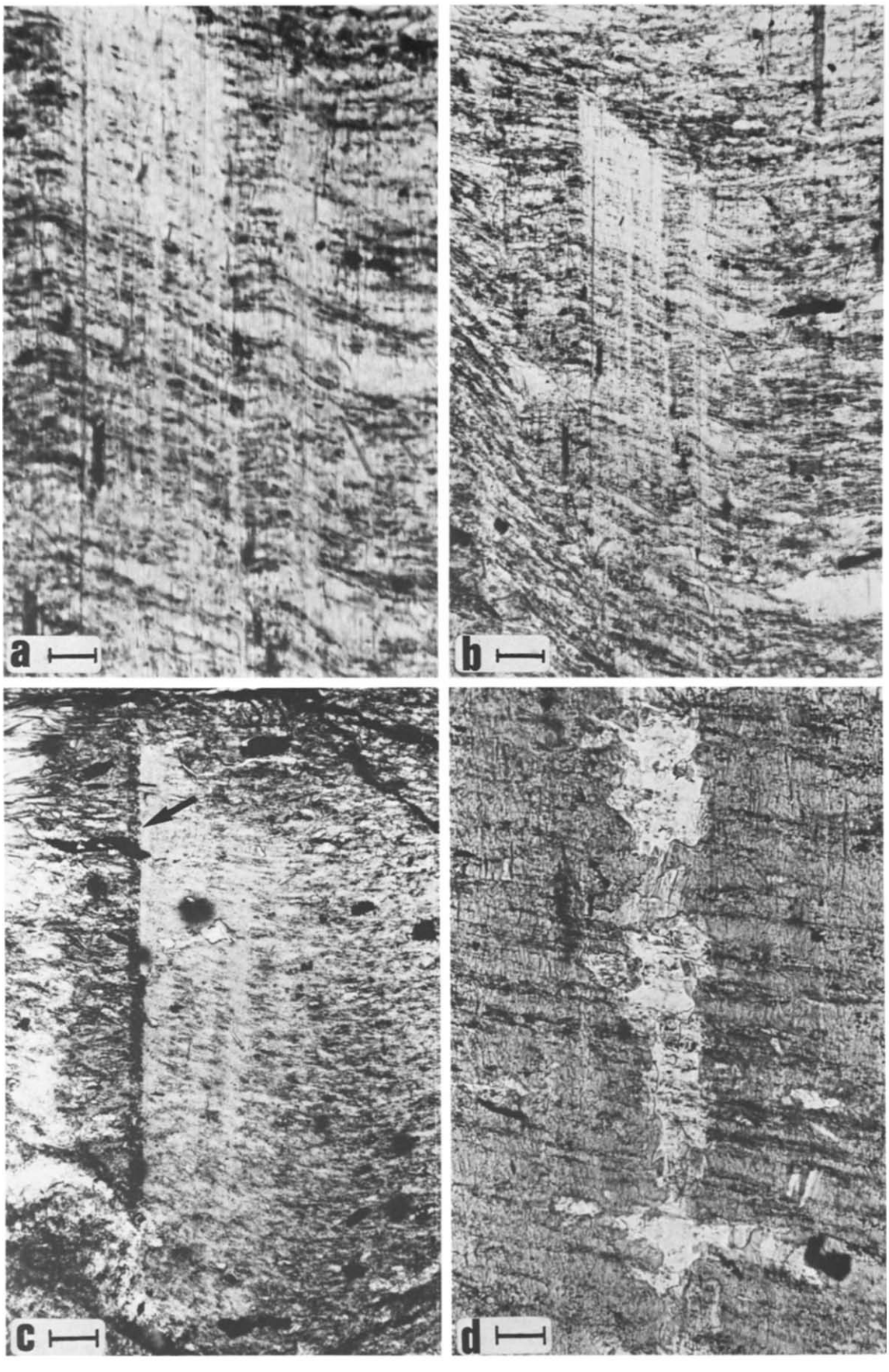

Fig. 9. Various banded-structures and lamellae in clear-zones are shown. In (a, b) inclusion trails are interrupted parallel to (001) by clear lamellae and sharp changes in curvature take place. Note the diffraction fringes caused by planar objects beyond the limits of optical resolution. At the edge of the 'clear' zone in (c) (see arrow) inclusions are concentrated on a surface dipping 40–50° into the section, parallel to (001). These inclusions were probably swept ahead of a migrating growth interface. In (d) an overgrown quartz-filled pressure shadow containing interrupted inclusion trails is shown. Note how the inclusion trails continue through this overgrown pressure-shadow back into the biotite blast. Scale bars: (a) 30 μm; (b) 60 μm; (c) 100 μm and (d) 30 μm.

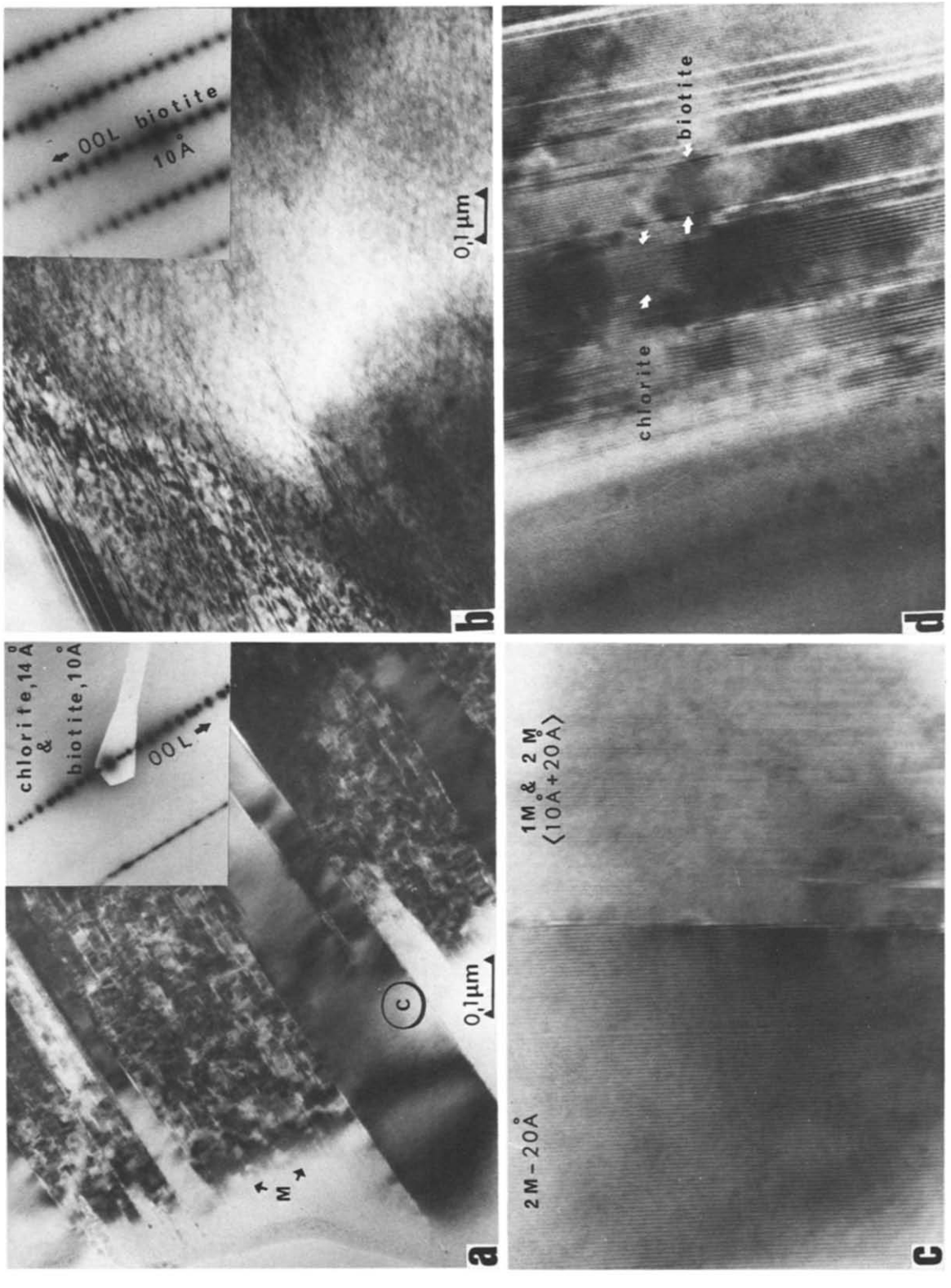

Fig. 10. Transmission electron micrographs of biotite blasts. In (a) a duplex region in the 'clear' zone consists of broad lamellae of chlorite (C), and 'mottled' bands (M) of intercalated chlorite and biotite. In (b) the central region of the blast is shown, with thin twins and stacking faults, but no chlorite. The diffraction contrast arises from electron-beam induced radiation damage. The inserts show the diffraction patterns of the respective areas. A high resolution electron micrograph (c) shows the interface region between 'C' and 'M' of diagram (a). The 1M and $2M_1$ polytypes are distinguished by the 10 and 20 Å fringe patterns. In (b) intercalation of 14 and 10 Å repeat-units represents the biotite and chlorite lamellae.

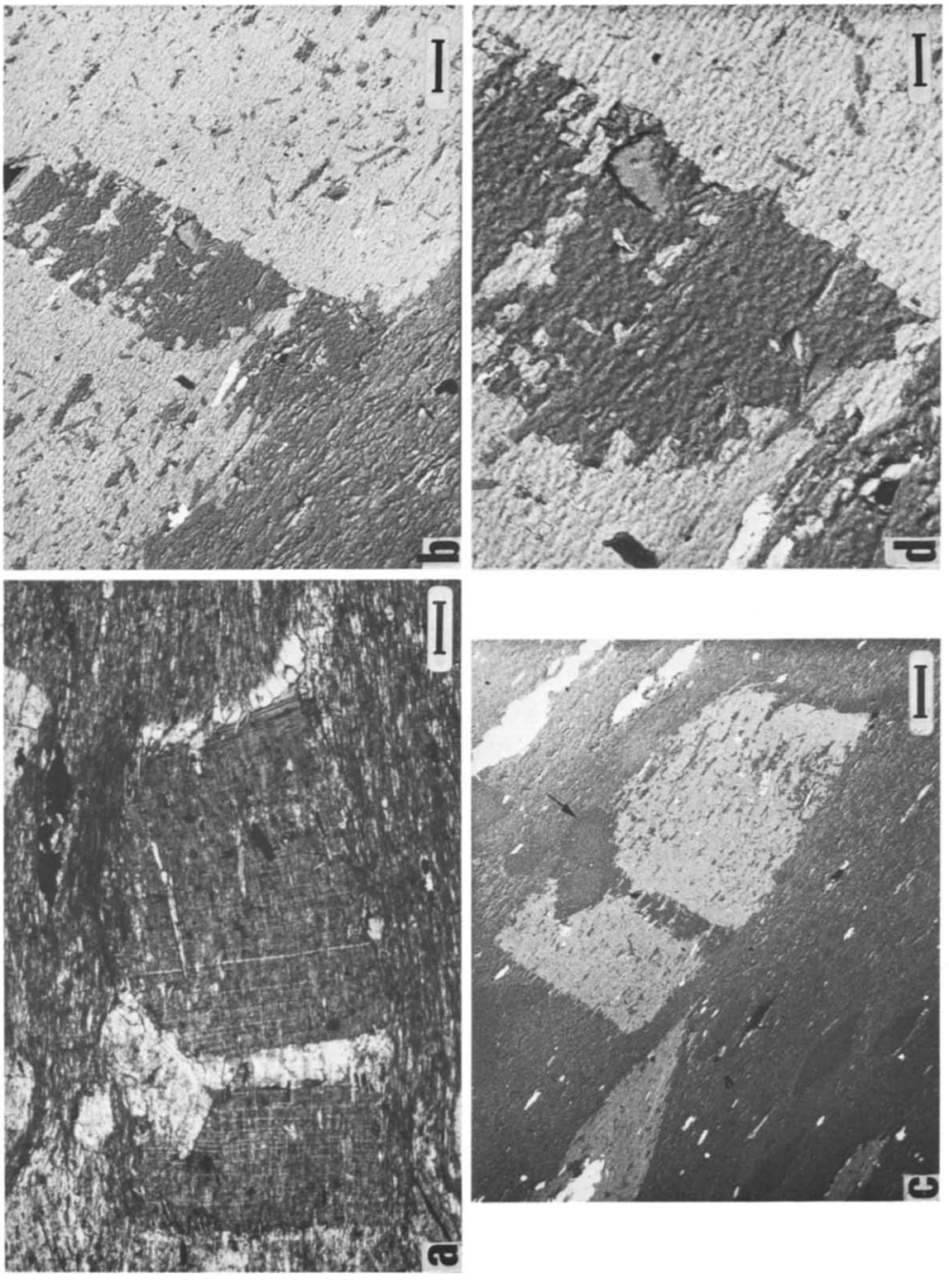

Fig. 12. A biotite blast with relatively coarse chlorite interbanding, contrasted as an optical (transmission) micrograph (a) and a Z-number contrast SEM image (b). The biotite has partially overgrown a zoned plagioclase blast (see text), and a cleavage-split pull apart has developed. In the pull-apart, there are many dentate and lamellar structures (c, d) often with interfaces parallel to the biotite (001). Scale bars: (a) 280 μm; (b) 400 μm; (c) 100 μm and (d) 40 μm.

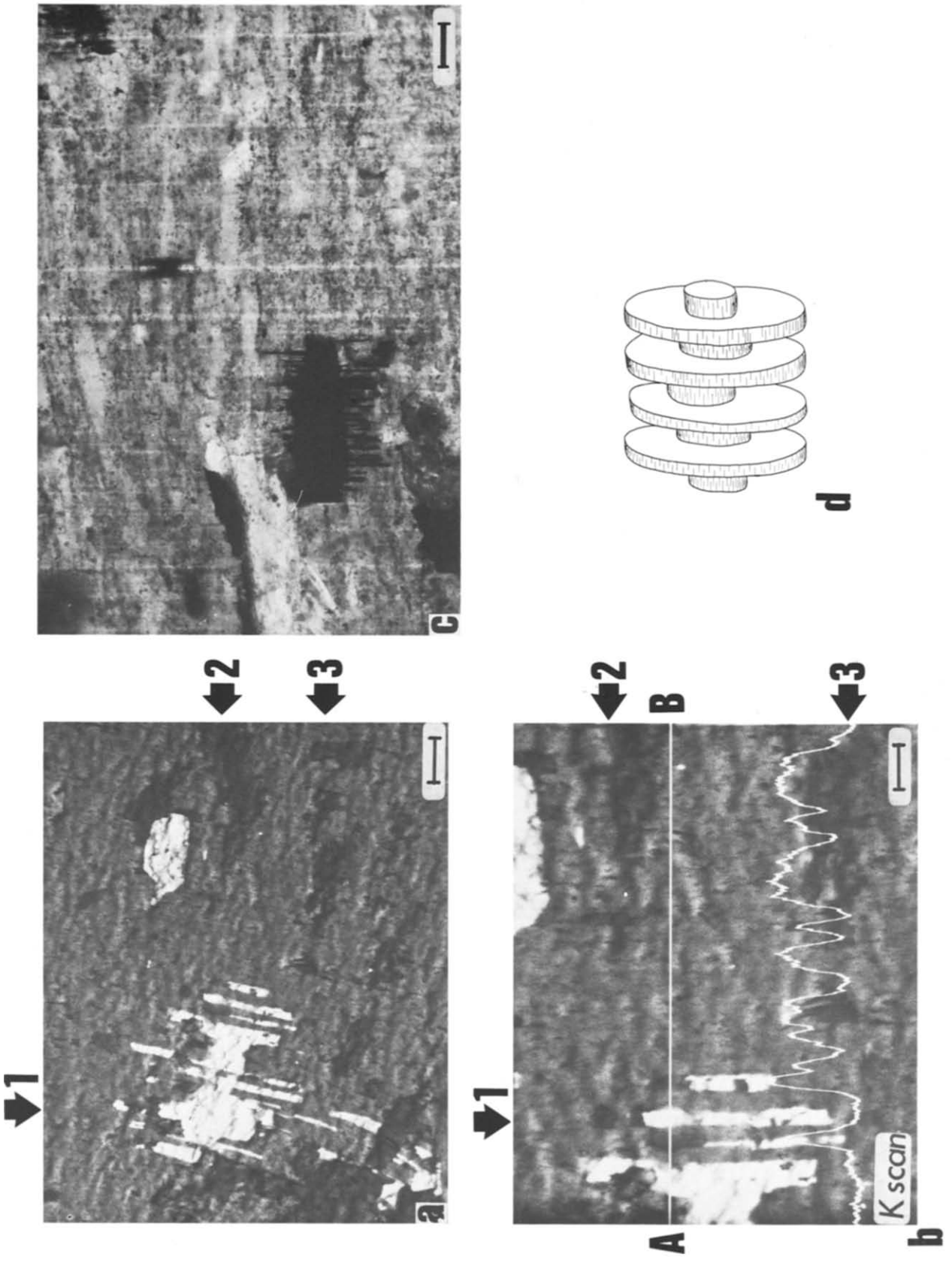

Fig. 13. (a, b) SEM Z-contrast images of biotite–chlorite intergrowths. Inclusions have 'radiator-fin' morphologies. Arrows at margins of (b) indicate inclusions of pyrite (1), quartz (2) and K-feldspar (3). Variation in potassium content was obtained by scanning the electron beam slowly over traverse AB in diagram (b). The darker chlorite bands correspond to dips in the K trace. Note rises corresponding to two K-feldspar lamellae. A spectacular 'radiator-fin' intergrowth of pyrite in the biotite–chlorite intercalations is shown in (c), with a three-dimensional representation of part of the inclusion shown in (d). Scale bars: (a) 20 μm; (b) 10 μm and (c) 80 μm.

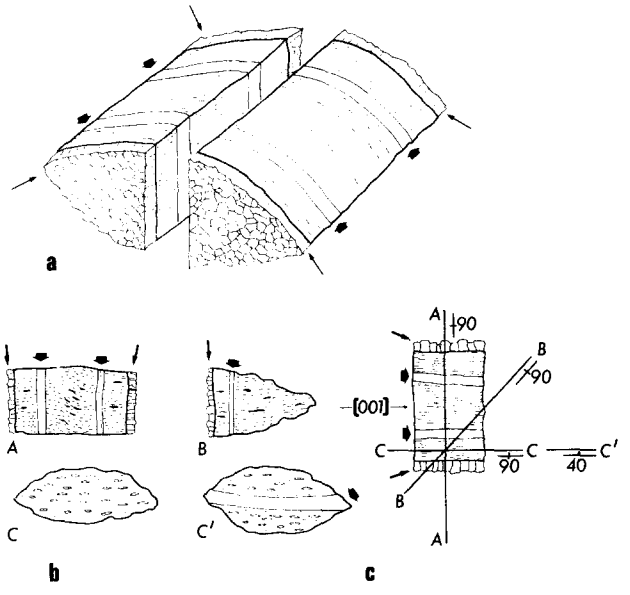

Fig. 5. (a) One typical blast morphology is shown in 3-D, in idealized form. The 2-D cut effects shown in (b) correspond to planes A, B, C and C', shown in diagram (c). The long arrows point to pressure shadows filled with quartz, chlorite and K-feldspar. The short arrows point to (001) parallel 'clear' zones.

Summary of microstructural characteristics

The blasts chosen for detailed microstructural analysis came from rocks in which S_1 appears to have remained in the extension field throughout the D_2 deformation. The most striking characteristics of these blasts are as follows.

(a) *Preferred blast morphology.* From the study of many thin sections it can be concluded that the blasts have two preferred morphologies, an idealized version of one of which is shown in Figs. 4 and 5.

(b) *Preferred crystallographic orientation.* Most blasts were oriented with the basal cleavage at 50–90° to the S_1 foliation plane, in the initial stages of growth. However, the traces of the basal planes show no preferred alignment in thin sections parallel to the foliation.

(c) *Inclusion trails.* Without exception the biotite blasts have inclusion trails inherited from the external foliation. The trails in the category of blasts examined are either planar or slightly 'S' or 'Z' shaped (Figs. 4a & b). These trails usually have the same asymmetry in all blasts in one thin section, and the trails curve into parallelism with the external foliation at the margin of the blast. Reversals of curvature of the inclusion trails are frequently observed. However, the inclination of the inclusion trails changes little along any particular biotite (001) plane.

(d) *'Clear' zones.* Zones that are relatively free of inclusions are found, usually parallel to the (001) plane (see Figs. 3–6). These 'clear' zones are usually paired, and occur symmetrically, at opposite ends of a blast (compare Figs. 3d, 4a & b and 6a).

(e) *Pressure-shadows.* There are usually pressure-shadows parallel to the (001) terminations of the blasts (Figs. 4 and 5), filled with quartz, chlorite, biotite, pyrite and K-feldspar (in order of decreasing significance). Pressure-shadows often have 'monoclinic' symmetry with respect to the centre of the blast (compare Figs. 4a and 6a).

(f) *Micro-boudinage and cleavage-split pull-apart structures.* These have many features in common with the pressure-shadows. The same minerals grew in these sites, though the percentage of biotite is highly variable. Biotite in these sites has not grown in optical continuity with the adjacent blasts, in marked contrast to the situation observed for paired 'clear' zones (see Fig. 6b). Rare instances of grain-boundary sliding have been observed (Fig. 6c), giving rise to a micro-dilation site in which biotite has grown on both sides of the opening grain boundary, in optical continuity with the host blast.

(g) *Dentate grain boundaries.* Biotites in the pressure-shadows are often columnar with dentate grain boundaries. The (001) planes are perpendicular to the direction of maximum growth. There is a greater tendency for grains to have columnar and/or dentate microstructures in cleavage-split pull-apart structures.

(h) *Various banded structures and lamellae.* Micro-veinlets sometimes link pressure-shadows and 'clear' zones in several successive blasts. In some of these 'clear' zones there are relatively thick lamellae (10–50 μm) of pyrite (Figs. 3b & c). A few blasts have 5–10 μm scale chlorite lamellae throughout, and a larger number have lamellae that are not optically resolvable.

(i) *The behaviour of chlorite in pressure-shadows.* Chlorites in pressure-shadows usually formed with (001) approximately parallel to the external foliation. Occasionally chlorites initiate inside the biotite blasts with (001) within 20° of the biotite (001) plane. These chlorites bend into the pressure-shadow, the (001) plane being rotated 60–80° over *c.* 10 μm until (001) is approximately parallel to the external foliation (Fig. 6d).

(j) *Kinks.* In many blasts minor kinking has taken place subsequent to growth. Frequently conjugate sets can be found.

BLAST MORPHOLOGY AND CUT EFFECTS

Blast morphology reflects growth history. In this case two different types of growth history can thereby be discerned, dependent on the initial orientation of the biotite (001) relative to the foliation S_1. All blasts examined initially overgrew a foliation inclined at 40–90° to the biotite (001). However, either of two blast morphologies then developed, depending on whether the biotite (001) was forward or back-inclined with respect to the local sense-of-shear. A tabular morphology

developed for blasts in which the biotite (001) was back-inclined, at 40–60° to S_1. This morphology is shown schematically in Fig. 5.

Considerable variation in the two-dimensional blast morphology results because thin-sections make different cuts through this 'ideal' blast morphology, as follows:

(a) A section which cuts a blast approximately perpendicular to the biotite (001) (plane A, Fig. 5) intersects the pressure shadows at the terminations of the blasts, and shows paired 'clear' zones and curved inclusion trails. The blasts are typically tabular or rectangular in this section (Figs. 4a & b).

(b) In a diagonal section so that the trace of (001) lies at high angles to the foliation trace (plane B, Fig. 5), the blasts appear asymmetric and the 'clear' zones are not paired (Fig. 4d). Typically there is a pressure-shadow at one end, a clear zone, then the blast narrows raggedly.

(c) A section through a blast approximately parallel to (001) (plane C, Fig. 5) shows the blasts as typically eye-shaped, and irregularly terminated. Inclusions are still elongate (Fig. 4c).

(d) In an oblique section so that the trace of (001) is parallel to the foliation trace (plane C', Fig. 5), blasts will again be eye-shaped, but because of the inclination of the cut, the 'clear' zones will intersect the section parallel to the foliation trace.

Apparent microstructural variations due to these cut effects can be eliminated in large part by considering only those blasts with (001) almost perpendicular to the plane of the thin section. This has been done for the rest of this paper.

THE INCLUSION TRAILS

The fine-grained inclusion trails in the blasts are defined by opaques including graphite, zircon and monazite (identified using SEM). Most of these have been included from the matrix as the blast grew. However the larger inclusions of quartz, K-feldspar and pyrite appear to have grown at the same time as the biotite. The inclusions often have segments parallel to (001) planes, or are interrupted parallel to (001) planes. This effect is shown particularly well in a polished thin section examined using scanning electron microscopy (compare Figs. 7a & b). There are two sorts of inclusions, one about 1–2 μm thick defining wispy trails, and others which are considerably larger and less frequent. Each of the micrographs (Figs. 7b–d) was obtained in the SEM using back-scattered electrons to create the image (Lloyd & Hall 1981). The image contrast in BEI (back-scattered electron imaging) mode is a function of the average atomic number of the material, and is hence commonly referred to as Z-number contrast or Z-contrast. The SEM images can be compared with the optical transmission micrograph (Fig. 7a).

Significance of the rotated inclusion trails

The rotated inclusion trails can be interpreted as indicating that the blast grew while the rock underwent mildly non-coaxial deformation, that is a flow with a simple shear component. Foliation-parallel shear (i.e. parallel to S_1) as the result of flexural slip during folding is suggested as the most likely cause of this non-coaxiality. Several authors have discussed the idea of a blast rotating while it grows. From the theoretical point of view, Lister & Williams (1983) have pointed out that a small round object in a flowing groundmass will spin, with respect to the local stretching axes, at a rate determined by the shear-induced vorticity, if flow couples the small round object to the average angular velocity of material lines radiating from the object. An estimate of the amount of shear strain undergone can thereby be made, with shear strain $\gamma = 0.7 - 1.0$ for blasts where the trails have rotated 20–30° and $\gamma = 2.5 - 2.8$ for blasts where maximum rotations (70–80°) were observed, assuming simple shear is the relevant deformation.

Growth history related to the kinematics of deformation

Supporting evidence in favour of non-coaxial flow producing the curved inclusion trails can be found in asymmetric pressure-shadows. These allow an independent assessment of the sense of shear, which is almost always consistent with that obtained using the curvature of the inclusion trails. This suggests that the bulk deformation was still often non-coaxial at the end of blastesis, with the same pattern of flow operating as during blastesis. However, the inclusion pattern in the blasts suggests that most rotation occurred before the paired 'clear' zones formed, so the paired 'clear' zones may have developed in what was effectively a period of post-shear extension, with the extension axis close to the foliation plane. In a number of blasts, reversals of the curvature of the inclusions trails occur (usually after the 'clear' zones formed), so actual reversals of shear sense may also have taken place subsequent to this period. Blastesis spanned a time interval including prograde and retrograde conditions, and it is not surprising if the local movement picture (perhaps related to flexural slip in a complex structure) changed during this time.

Blast shape related to initial orientation

As already demonstrated, the inclusion patterns in the blasts allow inferences to be made concerning their rotation and growth histories. We have already indicated that variation in morphology can be related to different initial orientations of the biotite (001) relative to the foliation S_1. The pattern of inclusions indicates that the blasts were thin (001) parallel plates in the initial stages of their growth, with (001) inclined at 40–90° to the foliation plane. These plates then expanded by growing perpendicular to (001), at the same time as they rotated with respect to the foliation. A fish-like shape developed (Fig. 3d and sequence a, b, c in Fig. 8), for initial orientations of the biotite (001) perpendicular to S_1, or if (001) was forward-inclined with respect to the local

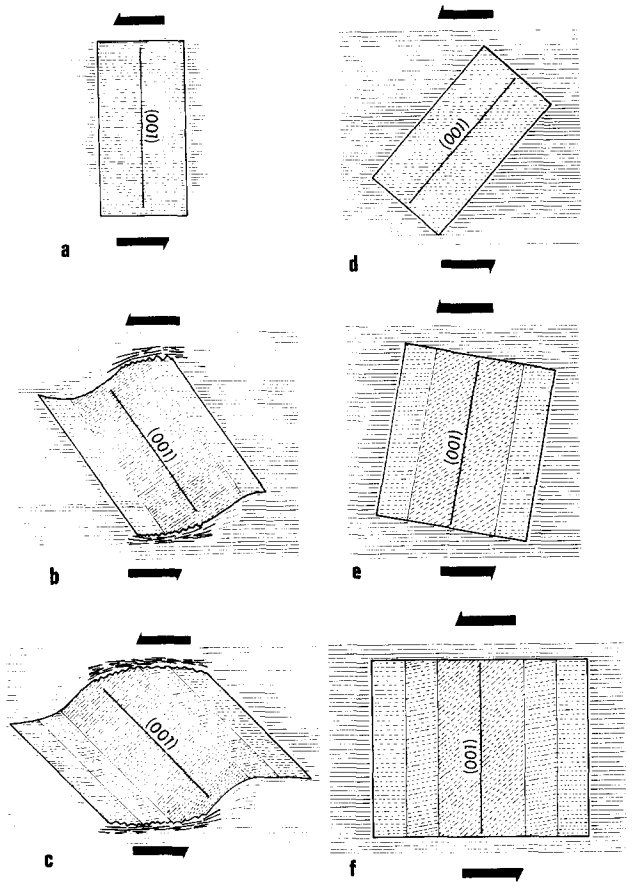

Fig. 8. The biotite blasts initiate with (001) at a high angle to S_1. The patterns in the inclusion trails suggest that the blasts were thin (001) parallel plates in their early stages. Two growth increments are shown for each of the three sequences, illustrating the variation in final blast morphology which results because of different starting orientations.

sense-of-shear. Tabular shapes (Figs. 4a & b) developed when the biotite (001) was back-inclined, relative to the local sense-of-shear, at 30–50° to S_1 (see sequence d, e, f in Fig. 8).

Blasts which initiate with (001) perpendicular to the foliation rotate so that the direction of maximum expansion remains in the shortening field, with the result as illustrated in sequence a, b, c in Fig. 8. The development of a fish-like habit is encouraged by rotation of the blast, since this increases normal stress on the sides of the blast parallel to S_1, and consequently pressure solution may remove biotite from these sites. Stylolitic residues develop (Figs. 8b & c) because of local mass removal in the matrix.

Blasts which initiate with (001) inclined at 40–60° to the external foliation rotate so that the direction of maximum expansion, perpendicular to (001), remains within the extension field of the flow. In terms of the development of the pressure-shadows, this means that space is always being created where it is needed to allow development of a tabular habit (see sequence d, e, f in Fig. 8).

ORIGIN OF THE PAIRED CLEAR ZONES

We turn now to consider the origin of the paired 'clear' zones, which are a common but distinctive feature of these blasts (Figs. 4 and 5). Paired 'clear' zones usually occur parallel to (001), near the (001) terminations of the blasts, and often exhibit 'monoclinic' symmetry with respect to the centre of the blast (Fig. 3d). Invariably the biotite in the 'clear' zone is in optical continuity with the biotite in the adjacent part of the blast.

Apart from the paired 'clear' zones, other types of 'clear' zones have formed in dilation sites caused by cleavage-split pull-aparts (Fig. 6b), by grain boundary sliding (Fig. 6c), or by the pulling apart of curved fracture planes. The clear biotite in these dilation sites has grown in optical continuity with the biotite in the adjacent blast. In contrast, in cleavage-split pull-aparts, the biotite is generally not in optical continuity with the adjacent blast. In such zones there are misorientations of up to 20° between the (001) planes of biotite in the 'clear' zones, and the (001) planes of biotite in torn-off sheets containing inclusions (Fig. 6d).

It is difficult to explain the paired 'clear' zones as cleavage-split pull-aparts. Cleavage-split pull-aparts have been recognized, but these are always in positions in agreement with theoretical predictions (Lloyd & Ferguson 1981, Lloyd *et al.* 1982) that extension fractures should occur more towards the centre of a blast. If the paired 'clear' zones are the result of dilational fractures in the blast, we have then to explain how these fractures managed to form symmetrically with respect to the centre of the blast. There are other dissimilarities in microstructure between the paired 'clear' zones and the cleavage-split pull-aparts. Inclusion trails often persist through 'clear' zones. This is not the case for pull-aparts (Fig. 6b). If inclusion trails are present in such zones, they are in (001)-bounded sheets of biotite torn from the walls of the cleavage-fracture during pull-apart (Fig. 6d). Therefore we reject this possibility, and describe specific microstructures which suggest an alternative origin for the paired 'clear' zones.

Banded structures and lamellae in the 'clear' zones

There are still inclusion trails in many of the paired 'clear' zones, but the density of inclusions is much less than in the surrounding biotites. The trails are often interrupted by inclusion-free lamellae parallel to (001). There are also zones parallel to (001) across which the density of inclusions in particular trails suddenly changes (Figs. 9a & b). Relatively abrupt changes in the orientation of the inclusion trails appear to coincide with these interruptions parallel to (001), and with the changes in inclusion density.

Opaque lamellae parallel to (001) in the 'clear' zones have already been mentioned, but there are also other lamellae parallel to (001) that are not optically resolvable (Fig. 9a). The latter have the characteristics of diffraction effects arising from tabular objects with a thickness smaller than the wavelength of light (i.e. less than *c.* 0.5 μm). This phenomenon is discussed further in the next section.

Sometimes at the margins of 'clear' zones there is a surface on which inclusions have been concentrated.

The surface shown in Fig. 9(c) dips at *c.* 50° into the section. The microstructure is suggestive of the sweeping of fine inclusions ahead of a migrating growth interface.

Microstructures of a 'clear' zone using TEM

The most direct way to determine the difference between a 'clear' zone and the adjacent biotite is to ion-thin a sample selectively from each area and to compare the microstructures in a TEM. The results of such a comparison are shown in Fig. 10. The biotite grain examined contains well-developed paired 'clear' zones, as illustrated previously in Fig. 4(b). The optically 'clear' zone consists of irregularly alternating layers of biotite and a second phase with a planar spacing of 14 Å, tentatively identified as a chlorite. The intercalation occurs parallel to the basal planes of the biotite. The orientation relationship of this phase with the biotite is shown in the indexed electron diffraction pattern.

This duplex (or two phase) microstructure (Fig. 10a) may be contrasted with the microstructure shown in Fig. 10(b) from the central region of the same biotite grain, in which the NE–SW narrow lamellae are stacking faults in the (001) planes of the biotite. The background contrast in this image arises from diffraction effects around lattice defects created by electron irradiation damage (Iijima & Buseck 1978). The chlorite phase (see Fig. 10a) did not normally damage as quickly as the biotite (Fig. 10b). The duplex structure seems to be confined to the 'clear' zones, at least in the grain examined in the TEM.

There are two other features of importance in the electron diffraction patterns: (a) the continuous streaking along (001) in reciprocal space indicates that the stacking sequence of the basal planes is not regular and (b) the individual diffraction spots are also streaked at right angles to (001), an effect which can be explained by refraction of electrons through small crystalline domains (see Gard 1976, p. 60, Heuer & Nord 1976, p. 348).

Stacking disorders are clearly seen within individual biotite regions. Figures 10(c) & (d) show images formed by interference between the central beam and two basal reflections one either side of it. Although these are not true structure images, they can nevertheless be used to detect anomalies in the basal plane stacking sequence (Iijima & Buseck 1978). The field of view is bisected by a boundary that separates a dominantly 20 Å repeat structure from a region consisting of mixed 10 and 20 Å repeat units. This observation establishes that the biotite has both 1M (10 Å c-repeat) and $2M_1$ (20 Å c-repeat) polytypes. The $2M_1$ regions damage very slowly in the beam.

TEM was also used to probe for differences in chemical composition. The spatial resolution attainable is about 0.05 μm, depending on the electron beam spot size. However, the accuracy of the analyses obtained is limited (Nord 1982, Champness *et al.* 1981). In the JEOL 200 C used for our analysis, the relative uncertainty on major elements is about ±10 weight percent. The composition of the host biotite, determined by conventional microprobe techniques, was used as an internal chemical standard. The results of analyses of the 'mottled' (M) and 'clear' (C) lamellae in a region of duplex structure are shown in Table 1. There are obvious differences between these lamellae. Initially it was thought that all C-lamellae were chlorite with the 14 Å c-repeat unit and the M-lamellae were duplex microstructures. However, this distinction is not unique since some of the C-lamellae may be the $2M_1$-polytype of biotite.

Table 1. Analytical electron microscopy of biotite

	Probe standard	Duplex structure mottled regions (M)	Duplex structure clear regions (C)
SiO_2	37	34	29
Al_2O_3	21	26	33
FeO	23	26	24
MgO	9	9	11
K_2O	9	5	2

Notes: (a) The results are given in terms of weight percentages, assuming an anhydrous phase in each case. The original probe results showed an average total of 94.3 per cent, the remainder was assumed to be water. (b) The small amount of TiO_2 (≈1.0%) in the original biotite is strongly partitioned in the duplex region. Most of the Ti is in the mottled lamellae.

The optical diffraction grating effect observed in these 'clear' zones (Fig. 9a) can now be explained by the presence of fine-scaled lamellae which act as phase objects of a size less than the wavelength of light. Their image width in the optical microscope is a function of the effective numerical aperture of the objective lens — see McLaren *et al.* (1970), Boland *et al.* (1977) for detailed analyses of these effects.

Growth of blasts into their own pressure-shadows

The above observations provide additional data suggesting that the paired 'clear' zones are primary growth structures. Since blastesis occurs symmetrically at both ends of the blast, it is suggested that the clear zones have formed as the result of the biotite blast expanding by growth into its own (continuously or discontinuously) dilating pressure-shadow. A pressure-shadow forms at the side of a 'rigid' object in a deforming polycrystalline aggregate because a fracture forms there and begins to open. This creates a dilation site in which minerals can nucleate and grow. The orientation of the growing biotite is controlled by the orientation of the biotite in the adjacent blast, for syntaxial growth, so optical continuity of the crystal structure can be expected (cf. Cox & Etheridge 1983). Examples of this process are given in Figs. 4(a) and 6(a) where paired 'clear' zones have formed in, or adjacent to, the pressure-shadow. In these two cases the 'clear' zones have not been later overgrown by biotite containing inclusions.

Tensional mode failure (Jaeger & Cook 1971) suggests the presence of a fluid in the grain boundary network (Etheridge 1983, Etheridge *et al.* 1984) with a pore pressure equal to or exceeding the least compressive stress. Increasing pore fluid pressure reduces the effective stress to a point where tensional mode fractures can

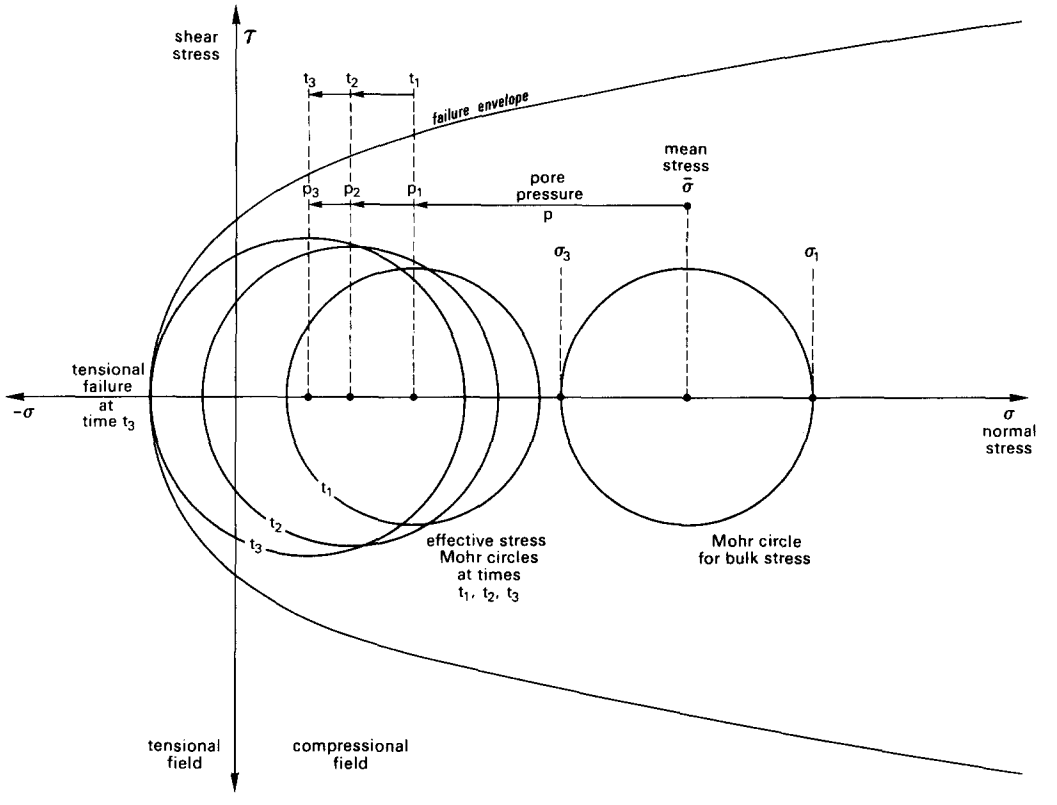

Fig. 11. Pore fluid pressure increasing in the grain boundary network drives the effective stress circle down the normal stress axis of the Mohr diagram, towards the failure envelope. We imagine a situation where the deviatoric stress is (temporarily) increasing, so the effective stress circle expands until finally at time, t_3, it reaches the failure envelope and tensional failure takes place.

form (Fig. 11). The fractures would localize at the sides of a blast because it is strong relative to the matrix. Tensional dilation of fractures can occur in all of the orientations we consider because: (a) local σ_1 axes can differ considerably in their attitude relative to the bulk σ_1 axis, because the blast acts as a stress guide, rotating the trajectories of the principal stress axes and (b) the bulk σ_1 axis need not be at 45° to S_1 to cause simple shear in an anisotropic material.

Note that the blasts may be relatively strong as a result of the abundance of fine grained impurity phases. In the adjacent Frédancon zone, clasts of impurity-rich biotite, obviously derived from these blasts, have survived in a matrix of recrystallized biotite, which contains few inclusions.

Formation of paired 'clear' zones

Consider now how continued growth of the biotite blast takes place, as the pressure-shadow fracture continues to dilate. Assume that growth occurs syntaxially. The growth interface will migrate into the dilating pressure-shadow cavity at a rate determined by the supersaturation Δc, where:

$$\Delta c = c - c_e,$$

with c, the actual concentration of the solution, and c_e the equilibrium concentration at the ambient P, T conditions (Brice 1973). Note that the equilibrium concentration, however, is also dependent on the properties of the growth interface. The value of Δc will depend on the supply of the necessary components from the matrix either by direct fluid flow or diffusive mass transport. The pressure-shadow fracture will dilate at a rate determined by the imposed strain rate and the size of the blast.

There are three possible outcomes for this model of the advance of a growth interface into a dilating pressure-shadow cavity: (a) if the matrix boundary recedes faster than the growth face advances, then the biotite cannot overgrow inclusions and a 'clear' zone will form; (b) if the matrix boundary is overgrown, the pressure-shadow fracture ceases to exist, although a new fracture may form at a later stage of growth — under these circumstances the biotite will overgrow inclusions; and (c) if the growth front reaches the matrix boundary and keeps pace with the dilation of the pressure-shadow fracture, inclusions from the matrix can be incorporated in the growing blast, or inclusions (insolubles such as graphite) from the matrix can be swept along ahead of the migrating growth front.

According to the above model, paired 'clear' zones would form when there is a perturbation in the growth rate and/or the strain rate. Either growth rate decreases or strain rate increases, so that the growth interfaces (located at both ends of the blast) advance more slowly than the matrix boundary recedes. 'Clear' zones thus form simultaneously at both ends of the blast.

Such conditions did not persist, since most paired 'clear' zones have a subsequent overgrowth of biotite containing inclusions. This implies that growth rate either accelerated, or strain rate decreased, subsequent

to the formation of the 'clear' zones, once again allowing the growth interface of the blast to reach the matrix boundary and overgrow inclusions. The banded structures in the 'clear' zones can be explained by periodic changes in the rate of growth related to component mobility or changes in strain rate. The relatively sudden changes in the orientations of the inclusion trails coincide approximately with the location of the 'clear' zones. This suggests sharp changes in the ratio of the magnitudes of growth rate versus spin of the blast, relative to external foliation. If deformation characteristics did not change abruptly, then the growth characteristics did so.

STEP-WISE DILATION OF THE PRESSURE SHADOW FRACTURE DURING BLASTESIS

There are many microstructures which suggest that the pressure-shadow fractures opened in a step-wise fashion, and in the last section of this paper we examine some of these in detail. Step-wise dilation of the pressure-shadow fracture is suggested by microstructures such as: (a) the many banded structures in the 'clear' zones; (b) the dentate grain boundaries exhibited by many inclusions and (c) 'radiator-fin' microstructures in pyrite, quartz and K-feldspar inclusions. These microstructures are very similar to those illustrated by Ramsay (1980) (see in particular Fig. 9(d) where a quartz filled pressure-shadow formed at an intermediate stage of blastesis and was subsequently overgrown). Note that the microstructure shown in Fig. 9(d) could not have formed in a step-wise dilating cleavage-split, since the inclusion trails pass through the quartz band. Rather, this microstructure suggests step-wise dilation of the pressure-shadow. Other microstructures suggest step-wise dilation of cleavage-split pull-aparts.

Microstructures of a cleavage-split pull-apart using SEM

One blast was selected for detailed examination with the SEM because it contained good examples of several microstructures indicating step-wise growth or step-wise dilation of pressure-shadows and cleavage-split pull-aparts. The blast selected for this study is shown in Figs. 12(a) & (b) as imaged in the optical microscope and in the SEM using BEI or the Z-contrast mode. Comparing the two types of images, the opaques in Fig. 12(a) are imaged as bright regions in Fig. 12(b); hence they represent high Z-material. From X-ray energy dispersive spot analyses, the high Z-materials were identified as zircons, monazites, xenotime and pyrite. The large opaques (in Fig. 12b) were identified as pyrite. The biotite is light grey in the Z-contrast image. The darker regions in the blast are inclusions of quartz, chlorite, K-feldspar, graphite, sphene and apatite.

This particular biotite blast has partially overgrown a zoned plagioclase blast (with an oligoclase core and an albite rim). The zoning was observed in the BEI image and confirmed by analyses of the Na and Ca contents across the blast. The oligoclase core has a higher effective Z-number because of its Ca content and so appears lighter in the BEI image. The oliogoclase core contains rotated inclusion trails, but in the albite rim these trails have the same attitude as the external foliation. The biotite blast grew after the oligoclase core formed, since the inclusion trails in the biotite blasts also are not rotated. This timing relationship suggests some biotite grew under retrograde conditions (i.e. decreasing T).

Possibly related to mechanical effects associated with the presence of the plagioclase blast, a cleavage-split pull-apart developed during blastesis and was filled with quartz, K–feldspar, biotite, chlorite and pyrite (Figs. 12 and 13). The grains in the pull-apart are columnar and a few grain boundaries are dentate. A banded structure is visible at the margin of the pull-apart with the matrix, and the inclusion trails in quartz are periodically interrupted. Similar dentate microstructures occur in the matrix adjacent to the pull-apart. Biotite is intergrown with chlorite, as can be seen by the alternation of lighter and darker bands in Z-contrast images (Figs. 13a & b) and in the optical micrograph (Fig. 13c). The dentate structures are clearly related to this alternation, as is evident in Fig. 13(a), which shows dentate intergrowths of pyrite (1) quartz (2) and K-feldspar (3). The 'radiator-fin' morphology (Fig. 13d) is best developed in pyrite, though it is present in the quartz and K-feldspar intergrowths as well. The similarities of microstructures in the pull-aparts and in the adjacent blast suggests the growth processes for both regions were similar, differing only in the ratios of the mobile species.

The chlorite lamellae in Figs. 12 and 13 are 1–10 μm thick. Since the spatial resolution for chemical variability is 2–3 μm in the SEM, a measure of the chemical variability across a region containing such lamellae can be obtained by scanning the electron beam slowly across the blast while monitoring the X-ray intensity for a selected element. For example, the K-scan line in Fig. 13(b) indicates the potassium variation along the trace line AB immediately above it. The two intense peaks at the left-hand side of the trace result from the K-feldspar inclusions intergrown with the pyrite. The other variations in K-content (i.e. the dips in the trace) appear to be related to the chlorite lamellae.

DISCUSSION

There are three aspects of this work which need further discussion. First there is the origin of the initial preferred orientation of the biotite. From the patterns exhibited by the inclusion trails, it can be inferred that the biotites began as thin (001) parallel plates oriented at high angles to the foliation. Second, there is the problem why during subsequent growth, expansion of the biotites took place parallel to the slow growth direction, perpendicular to (001), whereas the opposite might have been expected. Third, there is the question of a mechanism to explain how biotites grew into their own pressure-shadows.

Nucleation and growth

In general terms, two groups of mechanisms could be proposed to explain the initial oriented growth of the blast, classified by the categories 'oriented nucleation' or 'growth selection'.

Oriented nucleation could take place so that (001) was aligned parallel to the maximum compressive stress, σ_1. There are many demonstrations that such stress-controlled growth is theoretically possible (Kamb 1959, Paterson 1973). However for any specific situation, there are usually several other processes that can also explain the phenomena being discussed. In the present case, such alternative processes could involve random nucleation, and then selection of specific orientations as a result of the growth processes, that is in terms of a 'growth selection' hypothesis.

We suggest that the biotites initiated in fractures which then dilated to allow further growth. Biotites which nucleate with (001) parallel to the sides of a dilational fracture are in a favoured position for rapid initial growth. Growth selection will prevent continued growth of all nuclei except those nuclei with (001) parallel to the sides of the fracture. This hypothesis explains the initial preferred orientation of (001) at 40–90° to the foliation, since microfractures can be expected to have such orientations if σ_1 is oriented at high angles to the foliation plane.

The initial plate-like form of the blasts can thereby also be explained. Rapid growth parallel to (001) goes on only as long as there is free space. Blasts therefore initially have their long dimension parallel to (001). Expansion then takes place depending on the development of dilation sites in the pressure-shadow, at the sides of the blast parallel to (001). The blasts thus grow by expansion principally in directions perpendicular to (001). This process offers a ready explanation why the blasts commenced as thin (001) parallel plates (a shape long in the fast growth direction), and then expanded by growth perpendicular to (001), which is the slow growth direction.

Dilatancy-driven mass-pumping

The group of microstructures discussed in the previous section (p. 558) suggests that during blastesis a process was operative analogous to the crack-seal mechanism, proposed by Ramsay (1980) for step-wise dilation of veins. We have suggested that the biotite blasts grew, in part, by expanding into a discontinuously dilating pressure-shadow fracture. The step-wise growth increments vary from 100 Å to 1–2 μm. It is interesting to consider the physical conditions required for such a mechanism to take place. Earth scientists have become increasingly aware of the role of fluid in allowing mass-transport during deformation and metamorphism (Etheridge *et al.* 1983, 1984). Our observations necessitate reappraisal of the role of fluid in blastesis, as well as re-examination of the physical mechanism of blastesis itself. More than simple replacement is involved during growth of a porphyroblast.

Three basic models can be proposed to account for mass transport: (a) diffusion; (b) dilatancy-driven mass-pumping (described below); and advection (Etheridge *et al.* 1984). Theories concerned with the mechanism for pressure solution (see review by Rutter 1983) consider similar problems, and considerable discussion centres around the issue of the form of the 'pore fluid' in the grain-boundary networks. Models differ in their assumptions concerning the physical characteristics of the grain-boundary 'pore fluid', and in the properties of the fluid network. Matter can be assumed to be transferred by grain boundary diffusion (involving adsorbed monolayers, or structured boundary films), or via diffusion and/or actual fluid transport in a (free) pore fluid in a grain-boundary network consisting of (time statistically) connected channels or tubes. The microstructures reported in this paper suggest the transient existence of narrow fluid-filled cracks in a step-wise dilating pressure-shadow fracture. This fluid can be derived from a grain-boundary network of channels, tubes and lenses.

An argument that supports the existence of a pressurized pore fluid in the grain boundary network comes from the observation that tensional failure takes place during natural rock deformation (Etheridge 1983). Terzaghi's law of effective stress cannot be applied unless a pressurized pore fluid is present in sufficient quantities to affect the behaviour of microcracks. Since the permeability is likely to be very low, there is no reason to assume a high degree of (time statistical) connectivity in this grain-boundary fluid network. Significant variation in pressure in individual pore fluid lenses can be assumed to take place.

The deformation of rock in the presence of pore fluid is often accompanied by positive dilatancy which can cause a decrease in the pore pressure in the dilating zone. Hence there is a tendency for migration of the pore fluid towards this zone. The mechanism of seismic pumping proposed by Sibson (1977) considers a zone in which penetrative microcracking takes place, prior to the development of a macroscopic fracture. According to this model, the pore fluid pressure drops in the dilating microcracks, so the effective stress rises, and microcracking stops. The decreased pore pressure in the zone of microcracking drives the migration of pore fluid from the surrounding rocks towards the dilatant zone, so that pore pressure in the zone slowly rises, the effective stress drops, and microcracking once again commences. Urai (1983) has shown that the amount of dilatancy is to some extent controlled by the volume of the pore fluid reservoir.

The model above can be applied to the rocks considered in this paper, but only in modified form, because we are not dealing with penetrative microcracking prior to (catastrophic) failure. The rocks examined here were under P-T conditions which allowed ductile deformation to take place (as the result of diffusive mass transfer processes), and mineral growth presumably enabled microcracks to heal, so that no progressive increase in

dilatancy related to microcrack volume needs to be envisaged. At depth, prograde metamorphic reactions provided a continual supply of pore fluid which presumably migrated slowly upwards through the zone in which the biotite porphyroblasts grew.

Pressure oscillations in a continuously dilating microcrack need not take place, but since there is data for stepwise dilation, the question of oscillations of fluid pressure must be debated. In particular, the magnitude and frequency of the pressure drops is of interest. Tensional fractures spaced at intervals of 1 cm can relax accumulated elastic strains of 0.01% (less than 100 bars deviatoric stress) by dilating as little as 1 μm. The magnitude of the pressure drop will then depend on the rate of dilation of the pressure-shadow fracture, and the instantaneous permeability which determines the rate of fluid migration, as well as being affected by the amount of fluid in the vicinity of the fracture, and on the physical form and geometry of its dispersion in the grain boundary network. Relevant data necessary for the calculation include the time constants associated with (time-statistical) connectivity of the pore fluid in the grain boundary network, and its effective viscosity. Pore fluid pressure drops, comparable in magnitude to the ambient mean stress, can take place under favourable conditions.

Pore pressure drops in a dilating microcrack must be accompanied by periods in which the pore pressure slowly rises. The build-up in pore pressure can be the result of the flux of pore fluid from the metamorphosing regions at depth, or because dilatancy is relaxed by slow creep, diffusive mass transfer and mineral growth. In the case when the rock body is connected to a reservoir of pore fluid at higher pressure at depth, and when external influences continue to do mechanical work on the rock body, deviatoric stress and pore fluid pressure may both rise in the period preceding fracture. Figure 11 shows the effective stress circles for three successive time increments before tensional fracture takes place. Because pore pressure and deviatoric stress both increase, the effective stress circle is shown expanding as it is driven down the normal stress axis of the Mohr diagram, towards the failure envelope. At time t_3 the Mohr circle touches the failure envelope and tensional failure takes place. Pore fluid migrates into the opening fracture, and a pressure drop again takes place.

The solubility of silicates may decrease if an isothermal pressure drop takes place (Fyfe *et al.* 1978, Fournier & Potter 1982). If the pore fluid was saturated prior to the pressure drop, then opening of the pressure-shadow will coincide with the initiation of (relatively rapid) mineral growth. In the case of a step-wise dilating pressure-shadow fracture adjacent to a biotite porphyroblast, growth sites are provided by the blast and syntaxial growth of a platelet of biotite occurs. If there were inclusions in the biotite (e.g. quartz, K-feldspar, pyrite) these minerals keep growing. However, if the ratio of components has changed, for example from the last cycle of growth to the present one, the new growing platelets will occupy different relative areas. An inclusion of pyrite surrounded by biotite will then grow with a stepped or dentate grain boundary (Fig. 14), and inclusions with a 'radiator-fin' morphology (Fig. 13d) will result. Since, at the start of each step-wise dilation of the pressure-shadow fracture, the new growing minerals compete for the available surface area, 'radiator-fin' microstructures merely represent (discontinously) changing outcomes in the growth competition from one dilation increment to another.

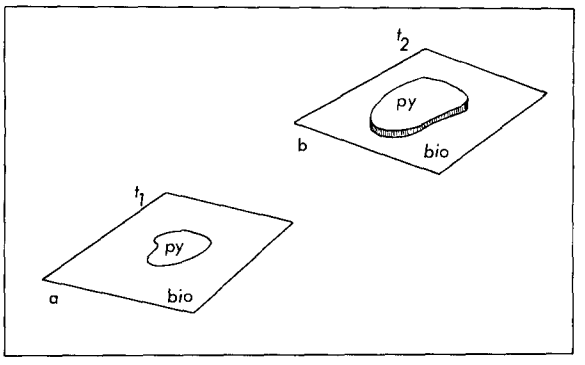

Fig. 14. In (a) the surface of the pressure-shadow fracture is shown before dilation followed by rapid crystal growth takes place. If the relative growth velocities of biotite and pyrite have changed from one dilation increment to the next, the relative size of the new grown platelet (b) will also change. This leads to dentate grain boundaries and in extreme cases the 'radiator-fin' microstructure.

The alternating growth of biotite and chlorite can be related to different phenomena. Growth of biotite during one dilation increment may depress the concentration level of one of the necessary components in the pore fluid. Diffusion of that component towards the blast may take place too slowly to prevent nucleation and (epitaxial) growth of a chlorite platelet during the next dilation increment. This phenomenon resembles the Leisegang effect (Fisher & Lasaga 1981) since it involves rhythmic attainment of a solubility product in a multicomponent system, and produces banded structures.

After the pressure-shadow fracture has stepped open, and mineral growth commenced, components diffuse or are transported down the pressure and concentration gradients in the surrounding grain boundary network towards the growth sites. Continued deformation may keep the pressure-shadow cavity opening, so that growth steps vary from 100 Å to 1–2 μm. If continuous dilation does not occur, this mineral growth slowly closes the pressure-shadow cavity, and fluid is expelled back into the grain boundary network. At the same time pore fluid pressure starts to rise, and the pore fluid becomes undersaturated. Because of the position in the cycle, and because the ratio of surface area to volume in the grain boundary network (as opposed to the ratio in the pressure-shadow fracture, dissolution will preferentially take place outside of the pressure shadow fracture, in the grain boundary network. In addition because pore fluid pressure starts to rise, the effective stress (σ_3-p) drops below zero towards the point where the pressure-shadow fracture will again step open (Fig. 15).

This cycling of pore pressure in the discontinuously dilating pressure-shadow fracture results in the opera-

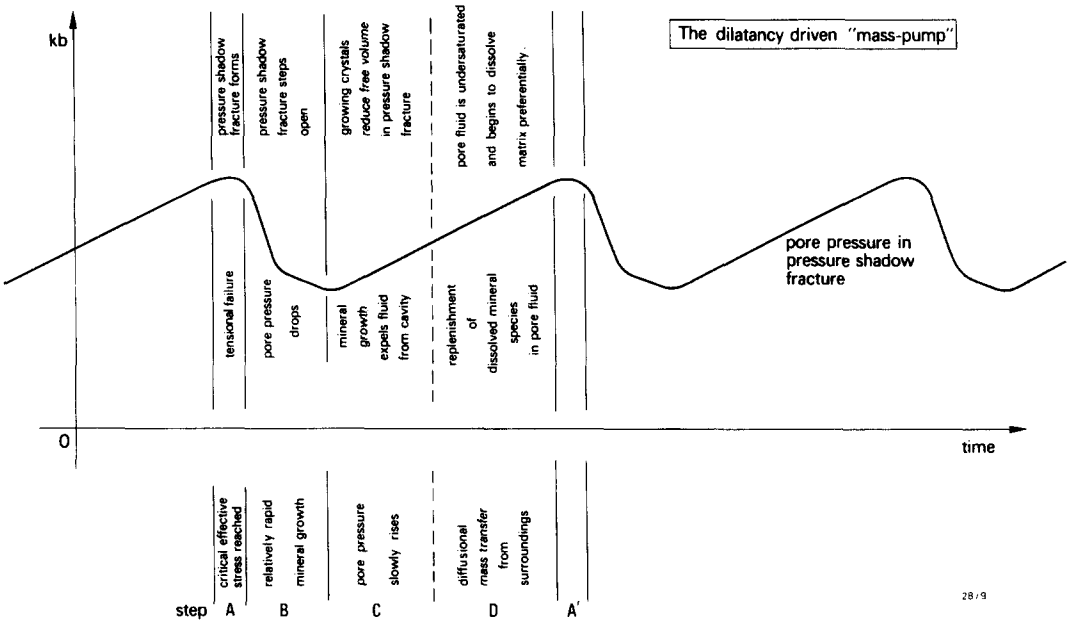

Fig. 15. The dilatancy driven 'mass pump' is a mechanism of mass transfer to dilatation sites, driven by effects related to variation of pore pressure caused by step-wise opening of fractures. A complete cycle involves: (A) dilation; (B) initially rapid mineral growth caused by a drop of pore pressure in the dilation site; (C) diffusion down pressure and concentration gradients to the growth site; (D) then as the fluid-filled cavity gradually closes, expulsion of fluid back into the grain boundary network and gradual rise in pore pressure. The pore fluid becomes undersaturated as this occurs, and solution once again takes place. Finally; (A') the critical effective stress needed to reactivate tensional failure is reached, and the pressure-shadow fracture once again steps open. Dilatancy mass-pumping offers an alternative to the classical pressure solution process.

tion of a dilatancy-driven 'mass pump'. The dilatancy-driven 'mass pump' has a cycle which involves crack formation, and mineral growth which attempts to close the crack. The efficiency of the 'mass pump' depends on the pressure-sensitivity of the relevant solubility products, and on the magnitude of the pressure oscillations in the pore fluid in the dilating pressure-shadow fracture.

CONCLUSIONS

(1) The biotite blasts formed during metamorphism of metapelites during early D_2. Significant deformation after blastesis was principally confined to the Frédancon movement zone, where transposition of S_1 took place. Outside this zone the rock deformed during D_2 by utilizing the pre-existing anisotropy (S_1) which was folded and crenulated.

(2) Biotites grew during both prograde and retrograde conditions. Intercalation of biotite and chlorite may be diagnostic for retrograde blastesis.

(3) The blasts initially grew with (001) at high angles to the S_1 cleavage. We propose that this is because the blasts nucleated in tension fractures which formed parallel to the maximum compressive stress σ_1, and that growth-selection led to the development only of nuclei with (001) parallel to the fracture wall.

(4) Curved inclusion trails in these blasts are related to rotation of the blasts with respect to the external foliation during growth. The rotation was caused by bulk non-coaxial deformation, suggested as due to S_1-parallel shear related to flexural slip during folding.

(5) Different three-dimensional blast shapes can be related to differences in initial orientation of (001) with respect to S_1, and the effects of growth during rotation. In the case of blasts with tabular shapes, the direction of maximum expansion, perpendicular to (001), remained in the extension field. In the case of blasts with fish-like shapes, the direction of maximum expansion remained in the shortening field. Pressure solution removed parts of these blasts during growth.

(6) Paired 'clear' zones in the blasts are related to growth of the blasts into the adjacent (continuously or discontinuously dilating) pressure-shadow fracture. A 'clear' zone results if the growth interface does not advance fast enough into the dilating pressure-shadow cavity to reach the receding matrix boundary.

(7) Evidence for step-wise dilation of the pressure-shadow fractures is provided by various microstructures (e.g. dentate grain boundaries, interrupted inclusion trails, sharp changes in the curvature of inclusion trails, and most importantly, the 'radiator-fin' microstructures exhibited by inclusions of quartz, K-feldspar and pyrite).

(8) These microstructures can be taken as evidence in support of a crack-seal mechanism for blastesis analogous to that proposed by Ramsay (1980) for vein formation. We suggest step-wise dilation of a pressure-shadow fracture into which the adjacent blast was itself growing. Narrow fluid-filled cavities probably had transitory existence in the dilating pressure-shadow fracture. The main effect of pressure drops may be to initiate rapid growth of a platelet of material in the fracture, thereby determining the microstructural characteristics of growth for the remainder of the dilation increment. This allows explanation of the 'radiator–fin' microstructures.

(9) A model is proposed for the transfer of mass during the cycling of pore pressure induced by step-wise dilation of features such as pressure-shadow fractures. It is assumed that periodic attainment of a critical effective stress for tensional failure is related to slow rise of pore pressure in the grain boundary network, as well as due to a tendency for deviatoric stress to rise if the pressure-shadow fractures are not dilating. Step-wise opening of the pressure-shadow fracture induces drops in pore pressure, which initiate periods of relatively rapid mineral growth in pressure-shadows cavities. Continued mineral growth then expels fluid back into the grain boundary network. As pore pressure slowly rises, the pore fluid becomes undersaturated, and dissolution of the matrix recommences, replenishing the fluid ready for the start of a new cycle of the dilatancy pump.

(10) This dilatancy-driven 'mass pump' will operate in any situation where cycling of pore pressure in the vicinity of a dilation site takes place, related to effects in the adjacent fluid-filled grain boundary network. It offers an alternative mechanism of mass transfer to the classical 'pressure solution' process.

Acknowledgements—We benefited from the work Prof. Dick Gilman, SUNY, Fredonia, U.S.A., carried out in this area in 1979–1980, and the conclusions he drew concerning the structure. We consulted with Hans de Bresser and Folkert Majoor who have arduously remapped the valley of the Rioumajou. Magda Martens is thanked for her efforts enabling production of this manuscript. Electron microscopy was performed on the ZWO-WACOM (The Netherlands Organisation for the Advancement of Pure Research) sponsored JEOL 200C on the Cambridge 150 SEM.

REFERENCES

Boland, J. N., Hobbs, B. E. & McLaren, A. C., 1977. The defect structure in natural and experimentally deformed kyanite. *Phys. Stat. Sol.* **39**, 631–641.

Brice, J. C. 1973. *The Growth of Crystals from Liquids.* Elsevier, New York.

Champness, P. E., Cliff, G. & Lorimer, G. W. 1981. Quantitative analytical electron microscopy. *Bull. Mineral.* **104**, 236–240.

Cox, S. F. & Etheridge, M. A. 1983. Crack–seal growth mechanisms and their significance in the development of oriented layer-silicate microstructures. *Tectonophysics* **92**, 147–170.

Clin, M., 1959. Étude geologique de la hautes chaines de Pyrenees centrales entre le cirque de trou mousses et du cirque du Lys. Thèse facultie des sciences, Nancy.

Etheridge, M. A. 1983. Differential stress magnitudes during regional deformation and metamorphism: upper bound imposed by tensile fracturing. *Geology* **11**, 231–234.

Etheridge, M. A., Wall, V. J. & Vernon, R. H. 1983. The role of the fluid phase during regional metamorphism and deformation. *J. Metamorphic Geology* **1**, 205–226.

Etheridge, M. A., Wall, V. J., Cox, S. F. & Vernon, R. H. 1984. High fluid pressures during regional metamorphism and deformation: implications for mass transport and deformation mechanisms. *J. geophys. Res.* **89**, 4344–4358.

Fisher, G. W. & Lasaga, A. C. 1981. Irreversible thermodynamics in petrology. In: *Reviews in Mineralogy*, vol. 8, '*Kinetics of Geochemical Processes*'. Mineralogical Society of America, 171–209.

Fournier, R. O. & Potter, R. W. II, 1982. An equation correlating the solubility of quartz in water from 25°C to 900°C at pressures up to 10,000 bars. *Geochim. cosmochim. Acta* **46**, 1969–1973.

Fyfe, W. S., Price, N. J. & Thompson, A. B. 1978. *Fluids in the Earth's Crust.* Elsevier, New York.

Gard, J. A. 1976. Interpretation of electron diffraction patterns. In: *Electron Microscopy in Mineralogy* (Edited by Wenk, H. R., Champness, P. E., Christie, J. M., Cowley, J. M., Heuer, A. H., Thomas, G. & Tighe, N. J.) Springer, Berlin, 52–67.

Heuer, A. H. & Nord, G. L. Jr. 1976. Polymorphic phase transitions in minerals. In: *Electron Microscopy in Mineralogy* (Edited by Wenk, H. R., Champness, P. E., Christie, J. M., Cowley, J. M., Heuer, A. H., Thomas, G. & Tighe, N. J.) Springer, Berlin 274–303.

Iijima, S. & Buseck, P. R. 1978. Experimental study of disordered mica structures by high-resolution electron microscopy. *Acta Cryst.* **A34**, 709–719.

Jaeger, J. C. & Cook, N. G. W. 1971. *Fundamentals of Rock Mechanics.* Chapman and Hall, London.

Kamb, W. B., 1959. Theory of preferred orientation developed by recrystallization under stress. *J. Geol.* **67**, 153–170.

Lister, G. S. & Williams, P. F. 1983. The partitioning of deformation in flowing rock masses. *Tectonophysics* **92**, 1–33.

Lloyd, G. E. & Ferguson, C. C. 1981. Boudinage structure — some new interpretations based on elastic–plastic finite element simulations. *J. Struct. Geol.* **3**, 117–126.

Lloyd, G. E. & Hall, M. G. 1981. Applications of scanning electron microscopy to the study of deformed rocks. *Tectonophysics* **78**, 687–698.

Lloyd, G. E., Ferguson, C. C. & Reading, K. 1982. A stress-transfer model for the development of extension fracture boudinage. *J. Struct. Geol.* **4**, 355–372.

McLaren, A. C., Turner, R. G., Boland, J. N. & Hobbs, B. E. 1970. Dislocation structure of the deformation lamellae in synthetic quartz; a study by electron and optical microscopy. *Contr. Miner. Petrol.* **29**, 104–115.

Nord, G. L., Jr. 1982. Analytical electron microscopy in mineralogy; exsolved phases in pyroxenes. *Ultramicroscopy* **8**, 109–120.

Paterson, M. S. 1973. Non-hydrostatic thermodynamics and its geologic applications. *Rev. Geophys. Space Phys.* **11**, 355–389.

Ramsay, J. G. 1980. The crack–seal mechanism of rock deformation. *Nature* **282**, 135–139.

Rutter, E. 1983. Pressure solution in nature, theory and experiment. *J. geol. Soc. Lond.* **140**, 725–740.

Schoneveld, C. 1977. A study of some typical inclusion patterns in strongly paracrystalline-rotated garnets. *Tectonophysics* **39**, 453–471.

Schoneveld, C. 1979. The geometry and the significance of inclusion patterns in syntectonic porphyroblasts. Unpublished thesis, University of Leiden.

Sibson, R. H. 1977. Fault rocks and fault mechanisms. *J. geol. Soc. Lond.* **133**, 191–213.

Trouiller, A. 1976. Les terrains Palaeozoiques de la vallée de Rioumajou (Pyrenees centrales) Thèse troisième cycle, Toulouse.

Urai, J. L. 1983. Deformation of wet salt rocks: an investigation into the interaction between mechanical properties and microstructural processes during deformation of polycrystalline carnallite and bischofite in the presence of a pore fluid. Unpublished Ph.D. thesis, Institute of Earth Sciences, University of Utrecht.

Zwart, H. J. 1962. On the determination of polymetamorphic mineral associations, and its applications to the Bosost area (central Pyrenees). *Geol. Rdsch.* **52**, 38–65.

Zwart, H. J. 1963. Some examples of the relations between deformation and metamorphism from the Central Pyrenees. *Geologie Mijnb.* **42**, 143–154.

Zwart, H. J. 1979. The geology of the central Pyrenees. *Leid. geol. Meded.* **50**, 1–47.